Tropopause Evolution in a Rapidly Intensifying Tropical Cyclone: A Static Stability Budget Analysis

Patrick Duran[*] and John Molinari

University at Albany, State University of New York, Albany, NY

[*]*Corresponding author address:* Department of Atmospheric and Environmental Sciences, University at Albany, State University of New York, 1400 Washington Avenue, Albany, NY.

E-mail: pduran2008@gmail.com

ABSTRACT

[8] We have some cool results!

1. Introduction

Perhaps introduce upper-tropospheric static stability and its relationship to the diurnal cycle before going into Patricia? Include references to Dunion, Navarro, and O'Neill here.

After undergoing a remarkably rapid intensification (RI), Hurricane Patricia (2015) set a new record as the strongest tropical cyclone (TC) ever observed in the Western Hemisphere (Kimberlain et al. 2016; Rogers et al. 2017). High-altitude dropsonde observations taken by the Tropical Cyclone Intensity (TCI) Experiment captured this RI in unprecedented detail (Doyle et al. 2017). These observations revealed remarkable changes in the structure of the cold-point tropopause and upper-level static stability as the storm intensified (Duran and Molinari 2018). At tropical storm intensity, shortly before RI commenced, a strong inversion layer existed just above Patricia's cold-point tropopause, which was located near 17.2 km. During the first half of the RI period, this inversion layer weakened throughout Patricia's inner core, with the weakening most pronounced over the developing eye. By the time the storm reached its maximum intensity, the inversion layer over the eye had disappeared almost completely, which was accompanied by an increase in the tropopause height to a level at or above the highest-available dropsonde data point (18.3 km) at two locations. Meanwhile over the eyewall region, the static stability re-strengthened and the tropopause was limited to a level at or below 17.5 km. The mechanisms that led to these changes in upper-level static stability and tropopause height are the subject of the current paper.

More recently, Dunion et al. (2014) documented a periodic oscillation of infrared brightness temperature in hurricanes, which they call the "TC diurnal pulse." There will be a whole bunch of papers cited here...

At some point (probably in the Discussion) mention the possible importance of static stability asymmetries, in the context of the Dunion diurnal pulse

3

2. Model Setup

The numerical simulations were performed using version 19.4 of Cloud Model 1 (CM1) described in Bryan and Rotunno (2009). The equations of motion were integrated on a 3000-km-wide, 30-km-deep axisymmetric grid with 1-km horizontal and 250-m vertical grid spacing. The computations were performed on an f-plane at 15°N latitude, over a sea surface with constant temperature of 30.5°C, which matches that observed near Hurricane Patricia (2015; Kimberlain et al. 2016). Horizontal turbulence was parameterized using the Smagorinsky scheme described in Bryan and Rotunno (2009, pg. 1773), with a prescribed mixing length that varied linearly from 100 m at a surface pressure of 1015 hPa to 1000 m at a surface pressure of 900 hPa. This formulation allows for realistically-large horizontal mixing lengths near the hurricane's inner core, consistent with the results of Bryan (2012), while not over-representing horizontal turbulence in convection at outer radii. Vertical turbulence was parameterized using the formulation of Markowski and Bryan (2016, their Eq. 6), using an asymptotic vertical mixing length of 100 m. A Rayleigh damping layer was applied outside of the 2900-km radius and above the 25-km level to prevent spurious gravity wave reflection at the model boundaries. Microphysical processes were parameterized using the Thompson et al. (2004) microphysics scheme and radiative heating tendencies were computed every two minutes using the Rapid Radiative Transfer Model for GCMs? (RRTMG) longwave and shortwave schemes (Iacono et al. 2008). A horizontally-homogeneous temperature and humidity field was initialized with a mean sounding computed using all dropsondes deployed during the TCI flight conducted within and around Tropical Storm Patricia on 21 October, 2015 (see Doyle et al. 2017 for details.) Above 19 km, where few TCI observations were available, the temperature profile was taken from the Climate Forecast System Reanalysis (CFSR) grid point nearest Patricia's storm center, valid at 18 UTC 21 October, 2015. Since relative humidity mea-

4

surements were unreliable at temperatures below -40°C (Bell et al. 2016), relative humidity was

set equal to 50% above 11.5 km (the level above which temperature dropped below -40°C). The

vortex described in Rotunno and Emanuel (1987, their Eq. 37) was used to initialize the wind

field, setting all parameters equal to the values used therein.

3. Budget Computation

The static stability can be expressed as the squared Brunt Väisälä frequency:

$$N_m^2 = \frac{g}{T}\left(\frac{\partial T}{\partial z} + \Gamma_m\right)\left(1 + \frac{T}{R_d/R_v + q_s}\frac{\partial q_s}{\partial T}\right) - \frac{g}{1 + q_t}\frac{\partial q_t}{\partial z}, \tag{1}$$

where g is gravitational acceleration, T is temperature, R_d and R_v are the gas constants of dry air

and water vapor, respectively, q_s is the saturation mixing ratio, q_t is the total condensate mixing

ratio, and Γ_m is the moist-adiabatic lapse rate:

$$\Gamma_m = DETERMINEWHATTHISISFORTHENON-CONSERVATIVEEQUATIONSET \tag{2}$$

In the tropopause layer, q_s, $\frac{\partial q_s}{\partial T}$, and $\frac{\partial q_t}{\partial z}$ approach zero. In this limiting case, Eq. 1 reduces to:

$$N^2 = \frac{g}{\theta_v}\frac{\partial \theta_v}{\partial z}, \tag{3}$$

where θ_v is the virtual potential temperature. To compute N^2, CM1 uses Eq. 1 in saturated

environments and Eq. 3 in sub-saturated environments; for mathematical simplicity, however,

only Eq. 3 will be used for the budget computations herein[1].

Taking the time derivative of Eq. 3 yields the static stability tendency:

$$\frac{\partial N^2}{\partial t} = \frac{g}{\theta}\frac{\partial}{\partial z}\frac{\partial \theta}{\partial t} + \frac{g}{\theta^2}\frac{\partial \theta}{\partial z}\frac{\partial \theta}{\partial t}, \tag{4}$$

where the potential temperature tendency, $\frac{\partial \theta}{\partial z}$, is:

$$\frac{\partial \theta}{\partial t} = HADV + VADV + HTURB + VTURB + MP + RAD + DISS \tag{5}$$

_____

[1]The validity of this approximation will be substantiated later in this section.

Each term on the right-hand side of Eq. 5 represents a potential temperature budget variable, each of which is output directly by the model every minute. HADV and VADV are the radial and vertical advective tendencies, HTURB and VTURB are the radial and vertical tendencies from the turbulence parameterization, MP is the tendency from the microphysics scheme, RAD is the tendency from the radiation scheme, and DISS is the tendency due to turbulent dissipation. This equation neglects Rayleigh damping, since this term is zero everywhere below 25 km, and the analysis domain does not extend to that height. Each term in Eq. 5 is substituted for $\frac{\partial \theta}{\partial t}$ in Eq. 4, yielding the contribution of each budget term to the static stability tendency. These terms are then summed, yielding an instantaneous "budget change" in N^2 every minute. These instantaneous budget changes are then averaged over 24-hour periods and compared to the total model change in N^2 over that same time period, i.e.:

$$\Delta N^2_{budget} = \sum_{t=t_0}^{t_0+\delta t} \frac{\partial N^2}{\partial t} \vert_t, NEEDBAROVERSUMMATION \qquad (6)$$

$$\Delta N^2_{model} = N^2_{t_0+\delta t} - N^2_{t_0}, \qquad (7)$$

where t_0 is an initial time and δ_t is 24 hours. In Eq. 6, Eq. 1 in saturated environments and Eq. 3 in sub-saturated environments; t_0 is an initial time and δ_t is 24 hours.

4. Results

Put description of Fig. 1 in this section.

Don't forget to mention 1-2-1 smoother.

a. Static stability evolution

The average N^2 over the first day of the simulation (Fig. 2a) indicates the presence of a static stability maximum about 400 m above the cold-point tropopause. This lower-stratospheric stable

layer had begun to erode during the initial spin-up period, with the maximum destabilitzation occurring at the innermost radii. This decrease in static stability continued into the second day of the simulation (Fig. 2b) as the storm intensified to hurricane strength (Fig. 1). Destabilization was particularly pronounced over the developing eye, where the time-mean cold-point tropopause height increased by up to 400 m compared to the previous day. Over the developing eyewall and outer rainband regions, meanwhile, the tropopause height remained nearly constant. During the third day of the simulation (Fig. 2c), static stability over the eye continued to decrease, and the cold-point tropopause height rose to 18.3 km at the storm center. The tropopause sloped sharply downward over the innermost radii, reaching the 16.4-km level near the 50-km radius. This local minimum in tropopause height corresponded to the eyewall region, where upper-tropospheric static stability increased during this time period. Outside of the eyewall region, static stability began to increase in the layer immediately overlying the cold-point tropopause. This stable layer sloped upward with radius, which corresponded to an upward-sloping tropopause radially outside of the eywall region. Over the next 24 hours (Fig. 2d), as the storm's maximum 10-m wind speed leveled off near 80 m s^{-1} (Fig. 1), the upper-tropospheric static stability within the eyewall region continued to strengthen, as did the static stability just above the cold-point tropopause radially outside of the eyewall. As the stable layer strengthened, its altitude rose slightly, which corresponded to a slight increase in tropopause height outside of the eyewall during this period. Within the upper troposphere radially outside of the eyewall, meanwhile, static stability decreased such that it was nearly neutral in a thin layer between the 120- and 150-km radii. The eye region likewise continued to destabilize, and the cold-point tropopause height increased to a level above 18.5 km. This static stability evolution closely follows that observed in Hurricane Patricia (2015; Duran and Molinari 2018).

7

b. Static stability budget analysis

The left column of Fig. 3 depicts 24-hour changes in N^2 over each of the four days of the simulation. These represent bulk changes computed by subtracting the instantaneous N^2 at the initial time from the instantaneous N^2 at the final time. The middle column of Fig. 3 represents the change in N^2 computed using Eq. XXX and the method described in Section 3. The residual between these two computations (Fig. 3, right column) is much smaller than the change in N^2, meaning that the budget peforms well within the analysis domain.

To determine which of the budget terms are most important, a time series of the contribution of each of the budget terms in Eq. XXX to the tropopause-layer static stability tendency is plotted in Fig. 4. For this figure, each of the budget terms is computed using the method described in Section 3, except with 1-hour averaging intervals instead of 24-hour intervals. The absolute values of these tendencies are then averaged over the radius-height domain depicted in Fig. 3 and plotted as a time series[2]. Advection (Fig. 4, red line) plays an important role in the mean tropopause-layer static stability tendency at all times, and vertical turbulence (Fig. 4, blue line) and radiation (Fig. 4, dark green line) both become important after 48 hours. Although the contribution from horizontal turbulence (Fig. 4, purple line) becomes more important after 72 hours, it is confined to a very small region immediately surrounding the eyewall tangential velocity maximum (not shown), and is negligible throughout the rest of the tropopause layer. The remaining two processes - microphysics and dissipative heating (Fig. 4, orange and light green lines, respectively) - lie atop one another near zero. These time series indicate that, at all times, three budget terms dominate the tropopause-layer static stability tendency: advection, vertical turbulence, and radiation. Variations

---

[2]It will be seeen in subsequent figures that each of the terms contributes both positively and negatively to the N^2 tendency within the analysis domain. Thus, taking an average over the domain tends to wash out the positive and negative contributions. To circumvent this problem, the absolute value of each of the terms is averaged, yielding a time series of the mean magnitude of each budget term.

in the magnitude and spatial structure of these terms drive the static stability changes depicted in Fig. 2; subsequent sections will focus on these variations and what causes them.

(i) 0-24 hours   The first 24 hours of the simulation was characterized by a weakening of the lower-stratospheric static stability maximum above 17 km (Fig. **??**a, purple shading) and an increase in static stability below (green shading). Although these tendencies extended out to the 200-km radius, they were particularly pronounced at innermost radii. A comparison of the contributions of advection (Fig. **??**b), vertical turbulence (Fig. **??**c), and radiation (Fig. **??**d) reveals that advection is primarily responsible for the change in static stability during this period. ...Explain this in the context of radial and vertical velocities...

(ii) 24-48 hours   During the second day of the simulation, the lower-stratospheric stable layer continued to weaken (Fig. 6a). This weakening trend in the 16.75-17.75-km layer extended from the 50 km radius outward to past 200 km, and was primarily driven by advection (Fig. 6b). Below this layer, static stability began to increse slightly. This stabilization had contributions from both vertical turbulence (Fig. 6c) and radiation (Fig. 6d) in the 16-16.5-km layer. ...Explain this in context of mean vertical mixing coefficient and mean radiative heating tendency... Meanwhile, radially inward of 60 km, static stability below 17.5 km continued to weaken, primarily due to advective processes.

(iii) 48-72 hours   The third day of the simulation marked a dramatic change in the structure of the tropopause-layer static stability tendencies. During this time, static stability increased markedly in an upward-sloping region within the 30-60-km radial band (Fig. 7a), and also increased within the 16.75-17.5-km layer out to at least the 200-km radius. As this layer stabilized, the layer immediately below it destabilized in a broad region extending from 60-200 km. Examination of the contribution from total advection (Fig. 7b) reveals that advection no longer dominates the

9

static stability tendencies. Instead, a combination of vertical turbulence (Fig. 7c) and radiation

(Fig. 7d) overcomes the destabilizing influence of advection to create the layer of increasing static

stability. Meanwhile, the destabilizing influence of vertical turbulence in a broad region below

17 km combines with a small region of destabilization due to radiation in the 50-120-km radial

band combine to destabilize the layer below 16.5 km in the 50-200-km radial band. Comparing

the sum of advection and vertical turbulence (Fig. 7e) to the sum of advection, vertical turbulence,

and radiation (Fig. 7f) reveals that radiation plays a fundamental role in the re-strengthening of the

lower-stratospheric stable layer during this time.

(iv) 72-96 hours

5. Discussion

Dunion et al. speculate that the diurna pulse only occurs in mature storms. Maybe the development of the near-tropopause stable layer could partially explain the reason for this.

References

Bell, M. M., and Coauthors, 2016: Office of Naval Research Tropical Cyclone Intensity (TCI) 2015 NASA WB-57 High Density Dropsonde Sounding System (HDSS) data, version 1.0. doi: 10.5065/D6KW5D8M.

Bryan, G. H., 2012: Effects of surface exchange coefficients and turbulence length scales on the intensity and structure of numerically simulated hurricanes. *Mon. Wea. Rev.*, **140**, 1125–1143.

Bryan, G. H., and R. Rotunno, 2009: The maximum intensity of tropical cyclones in axisymmetric numerical model simulations. *Mon. Wea. Rev.*, **137**, 1770–1789.

Doyle, J. D., and Coauthors, 2017: A view of tropical cyclones from above: The Tropical Cyclone Intensity (TCI) Experiment. *Bull. Amer. Meteor. Soc.*, **98**, 2113–2134.

Dunion, J. P., C. D. Thorncroft, and C. S. Velden, 2014: The tropical cyclone diurnal cycle of mature hurricanes. *Mon. Wea. Rev.*, **142**, 3900–3919.

Duran, P., and J. Molinari, 2018: Dramatic inner-core tropopause variability during the rapid intensification of Hurricane Patricia (2015). *Mon. Wea. Rev.*, **XXX**, XXX–XXX.

Iacono, M. J., J. S. Delamere, E. J. Mlawer, M. W. Shephard, S. A. Clough, and W. D. Collins, 2008: Radiative forcing by long-lived greenhouse gases: Calculations with the AER radiative transfer models. *J. Geophys. Res.*, **113 (D13103)**.

Kimberlain, T. B., E. S. Blake, and J. P. Cangialosi, 2016: Tropical cyclone report: Hurricane Patricia. National Hurricane Center. [Available online at www.nhc.noaa.gov].

Markowski, P. M., and G. H. Bryan, 2016: LES of laminar flow in the PBL: A potential problem for convective storm simulations. *Mon. Wea. Rev.*, **144**, 1841–1850.

Rogers, R. F., S. Aberson, M. M. Bell, D. J. Cecil, J. D. Doyle, J. Morgerman, L. K. Shay, and C. Velden, 2017: Re-writing the tropical record books: The extraordinary intensification of Hurricane Patricia (2015). *Bull. Amer. Meteor. Soc.*, **98**, 2091–2112.

Rotunno, R., and K. A. Emanuel, 1987: An air-sea interaction theory for tropical cyclones. Part II: Evolutionary study using a nonhydrostatic axisymmetric numerical model. *J. Atmos. Sci.*, **44**, 542–561.

Thompson, G., R. M. Rasmussen, and K. Manning, 2004: Explicit forecasts of winter precipitation using an improved bulk microphysics scheme. Part I: Description and sensitivity analysis. *Mon. Wea. Rev.*, **132**, 519–542.
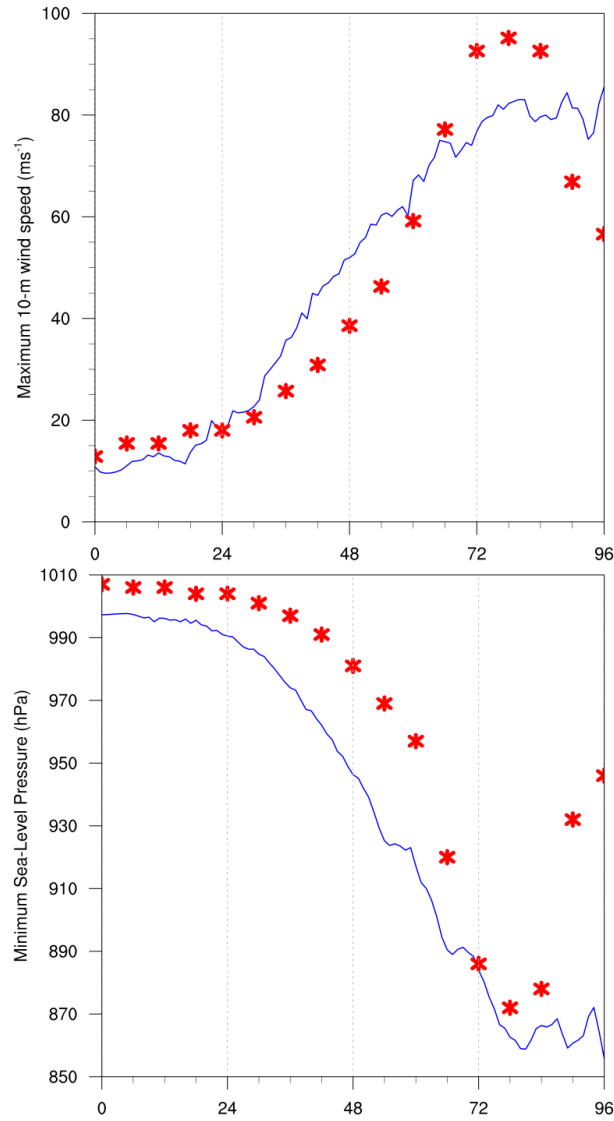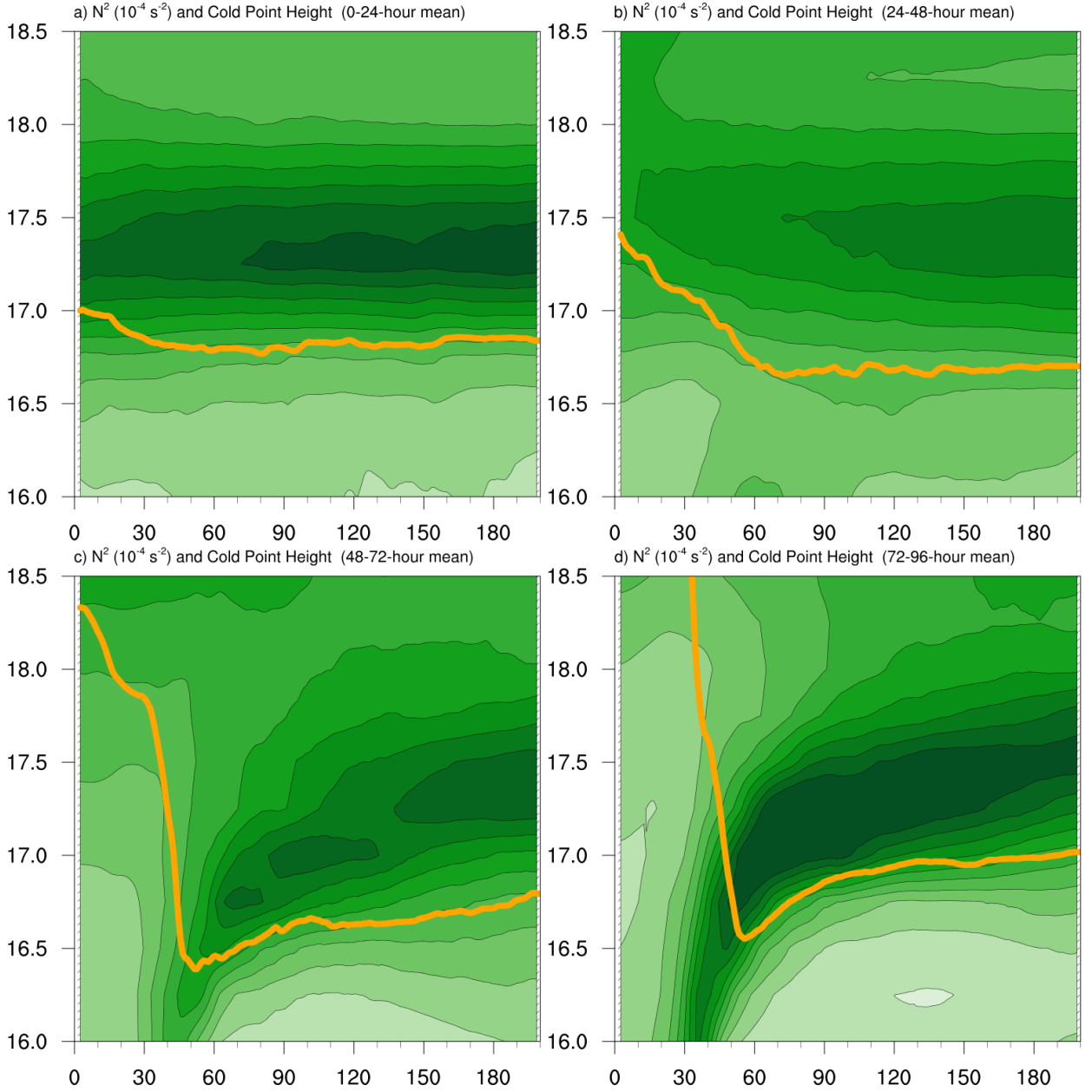
LIST OF FIGURES

FIG. 1. The maximum 10-m wind speed (top panel; m s^{-2}) and minimum sea-level pressure (bottom panel; hPa) in the simulated storm (blue lines) and from Hurricane Patricia's best track (red stars).

FIG. 2. Twenty-four-hour averages of squared Brunt-Väisälä frequency (10^{-4} s^{-2}) over the first four days of the simulation. Orange lines represent the cold-point tropopause computed from the mean temperature field over the same time periods.
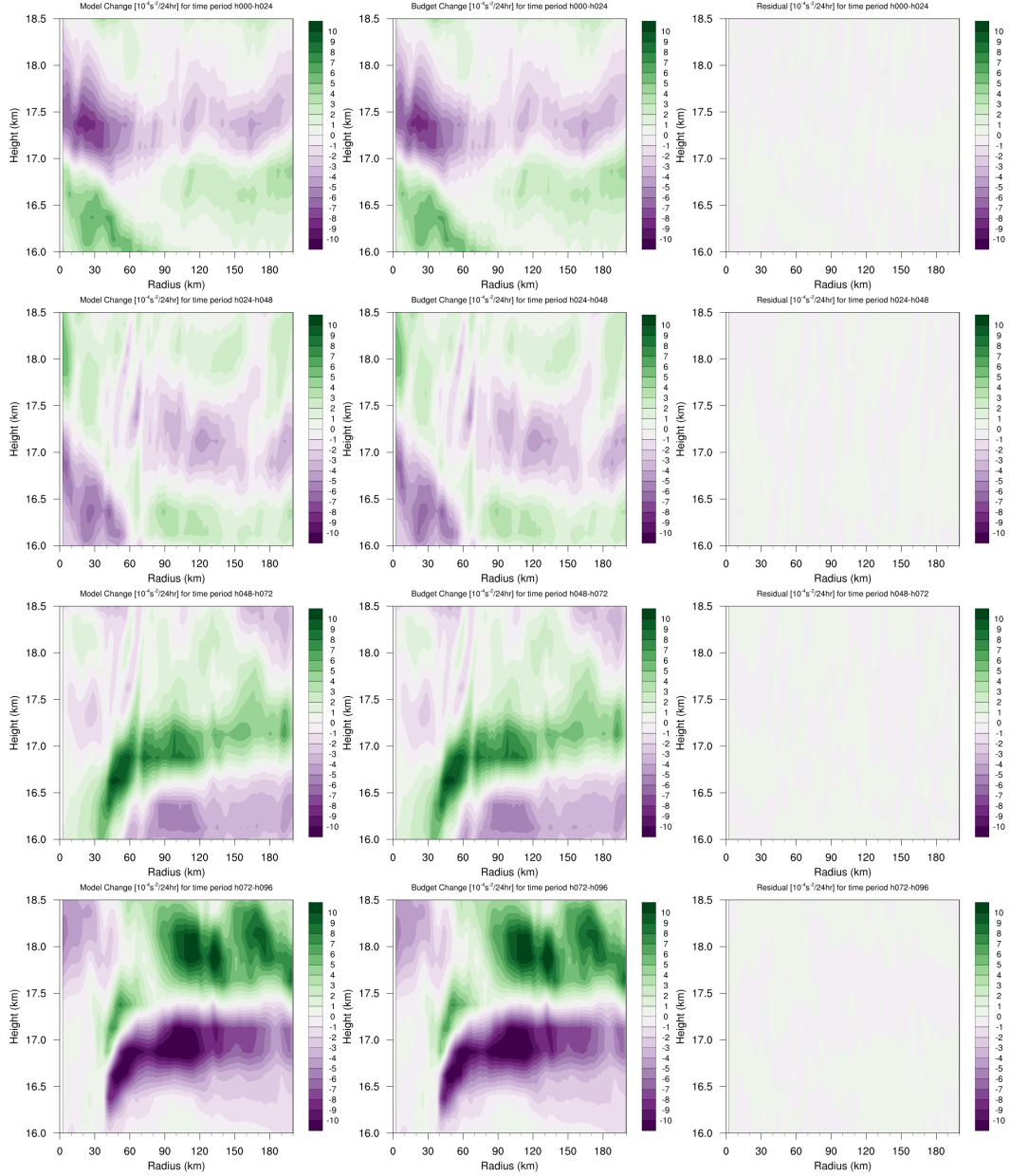
FIG. 3. Left panels: Twenty-four-hour changes in squared Brunt-Väisälä frequency (10^{-4} s^{-2}) over (a) 0-24 hours, (b) 24-48 hours, (c) 48-72 hours, (d) 72-96 hours. Middle Panels: The N^2 change over the same time periods computed using Eq. XXX. Right Panels: The budget residual over the same time periods, computed by subtracting the budget change (middle column) from the model change (left column).

1-hour averages of $|\Delta N^2|$ for each budget term in layer 16.0-18.5 km
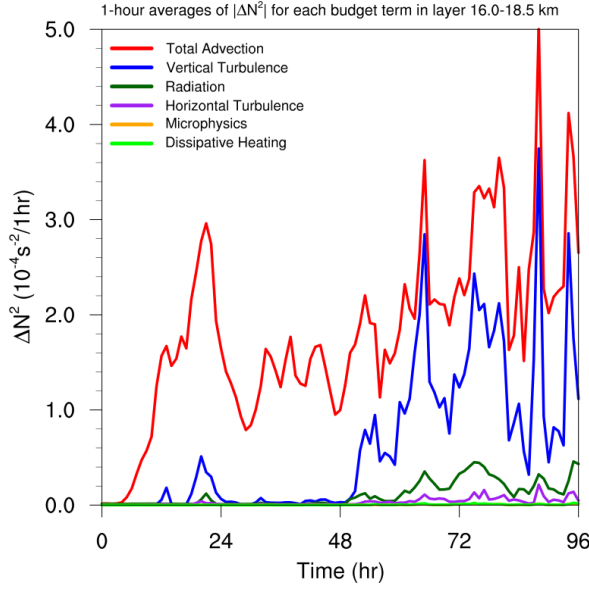
FIG. 4. Time series of the contribution of each of the budget terms to the time tendency of the squared Brunt-Väisälä frequency (N^2; 10^{-4} s^{-2}). For each budget term, the absolute value of the N^2 tendency is averaged both temporally over 1-hour periods (using output every minute), and spatially within the radius-height domain depicted in Fig. 3.
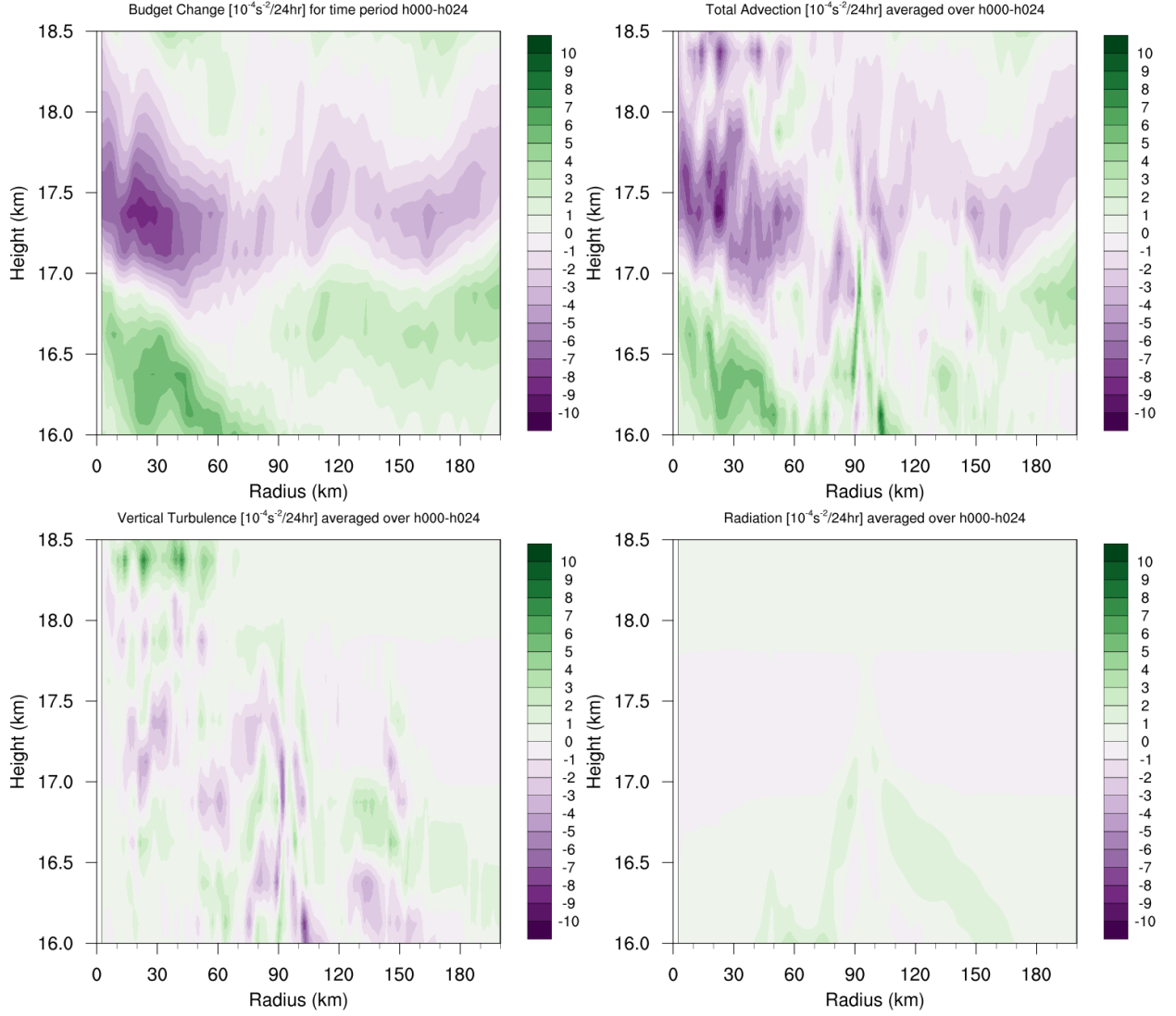
FIG. 5. (a) Total change in N^2 over the 0-24-hour period (10^{-4} s^{-2} (24 hr)$^{-1}$) and the contributions to that change from (b) the sum of horizontal and vertical advection, (c) vertical turbulence, and (d) the sum of longwave and shortwave radiation.
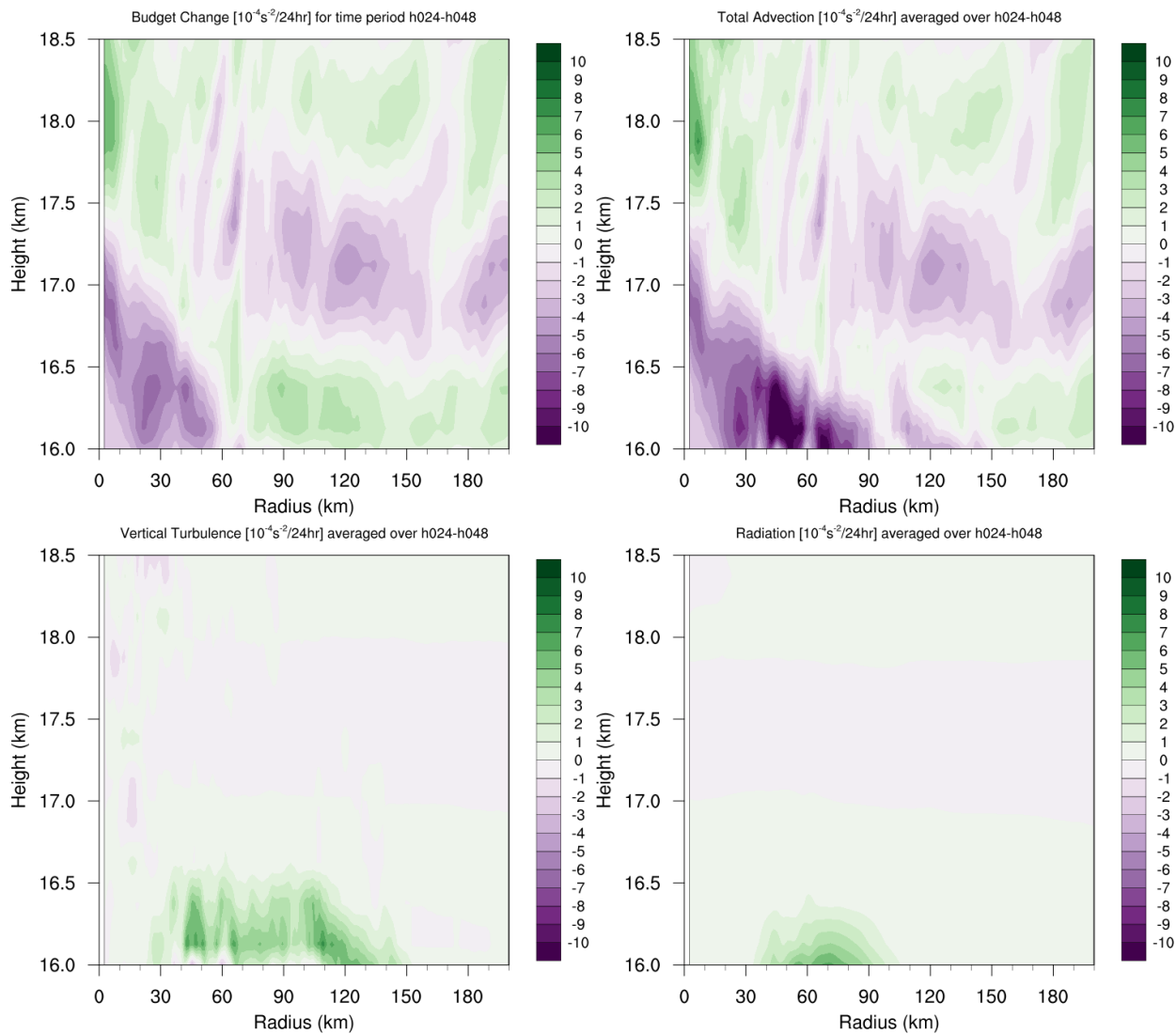
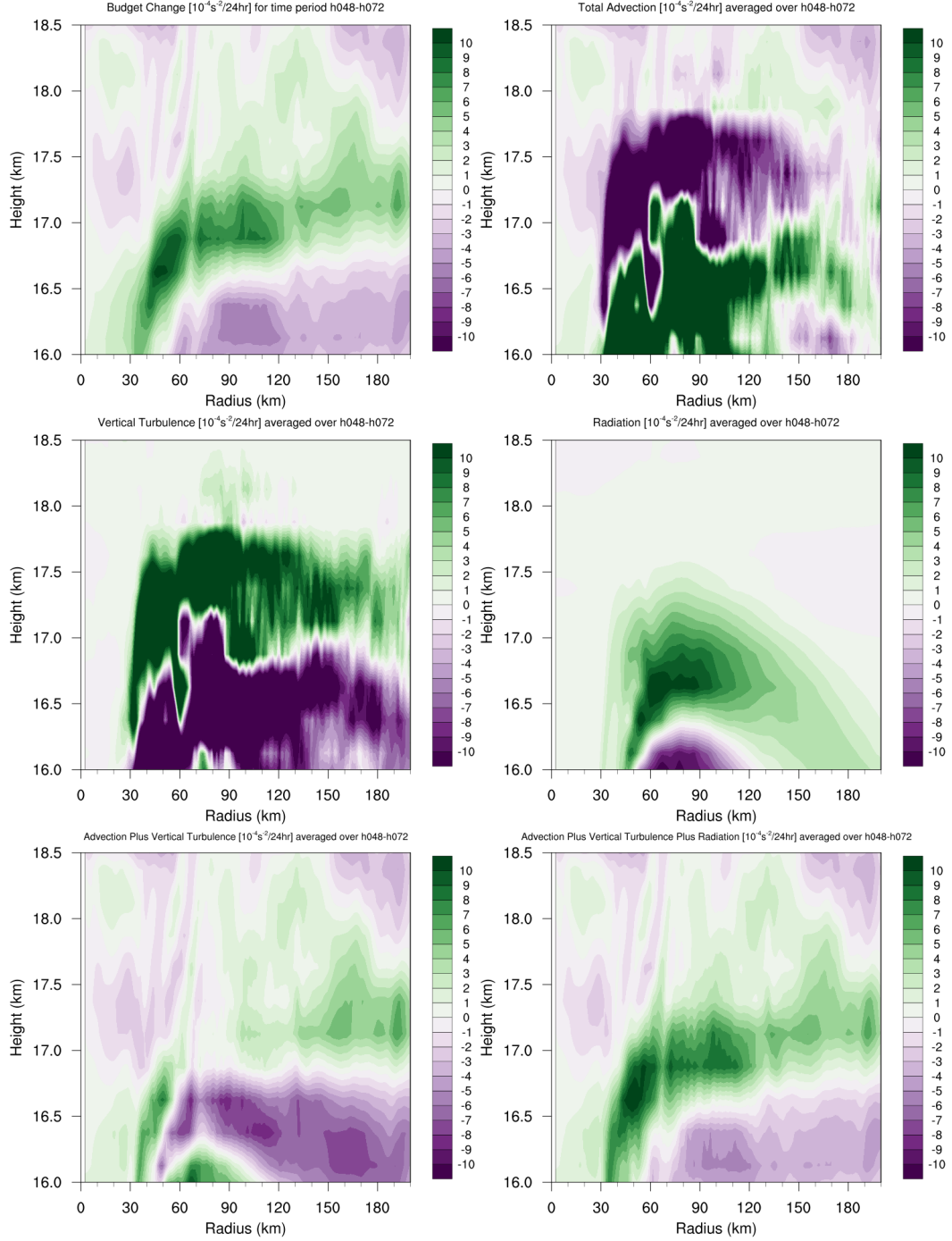FIG. 6. As in Fig. 5, but for the 24-48-hour period.

FIG. 7. (a) Total change in N^2 over the 48-72-hour period (10^{-4} s^{-2} (24 hr)$^{-1}$) and the contributions to that change from (b) the sum of horizontal and vertical advection, (c) vertical turbulence, (d) the sum of longwave and shortwave radiation, (e) the sum of horizontal advection, vertical advection, and vertical turublence, and (f) the sum of horizontal advection, vertical advection, vertical turbulence, and longwave and shortwave radiation.
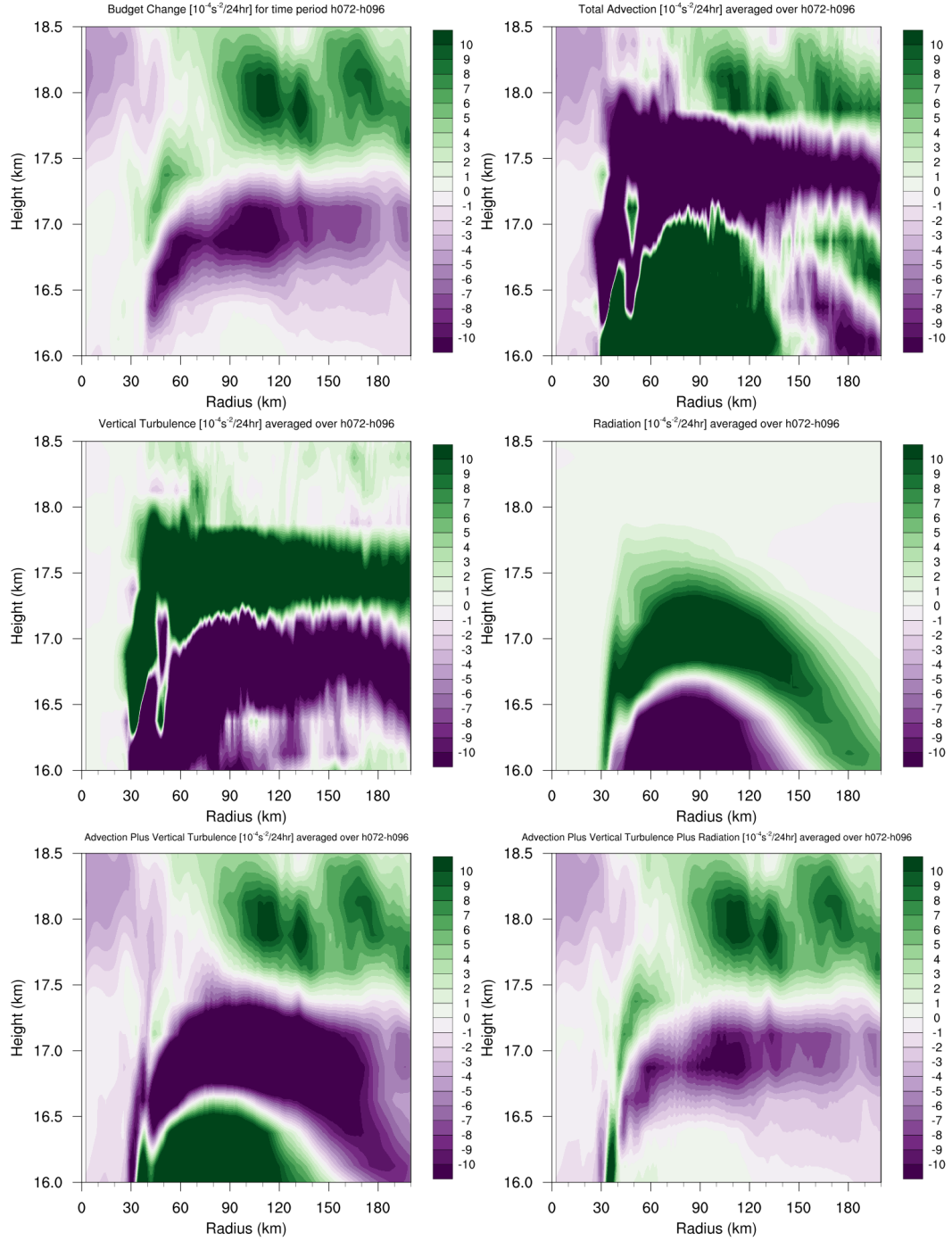
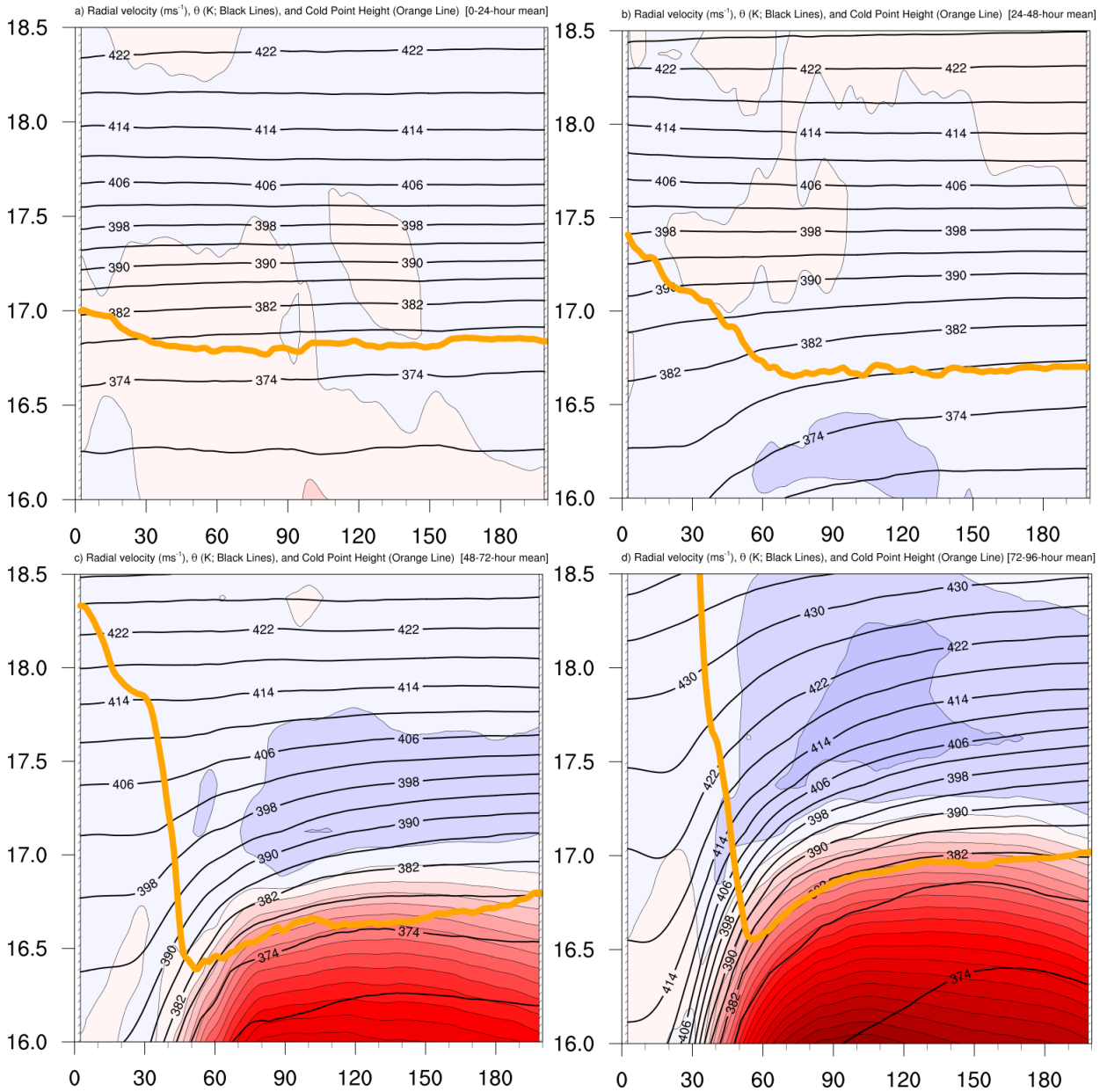FIG. 8. As in Fig. 7, but for the 72-96-hour period.

FIG. 9. Radial velocity (m s^{-1}; filled contours), potential temperature (K; thick black contours), and cold point tropopause height (orange line) averaged over (a) 0-24 hours, (b) 24-48 hours, (c) 48-72 hours, and (d) 72-96 hours.
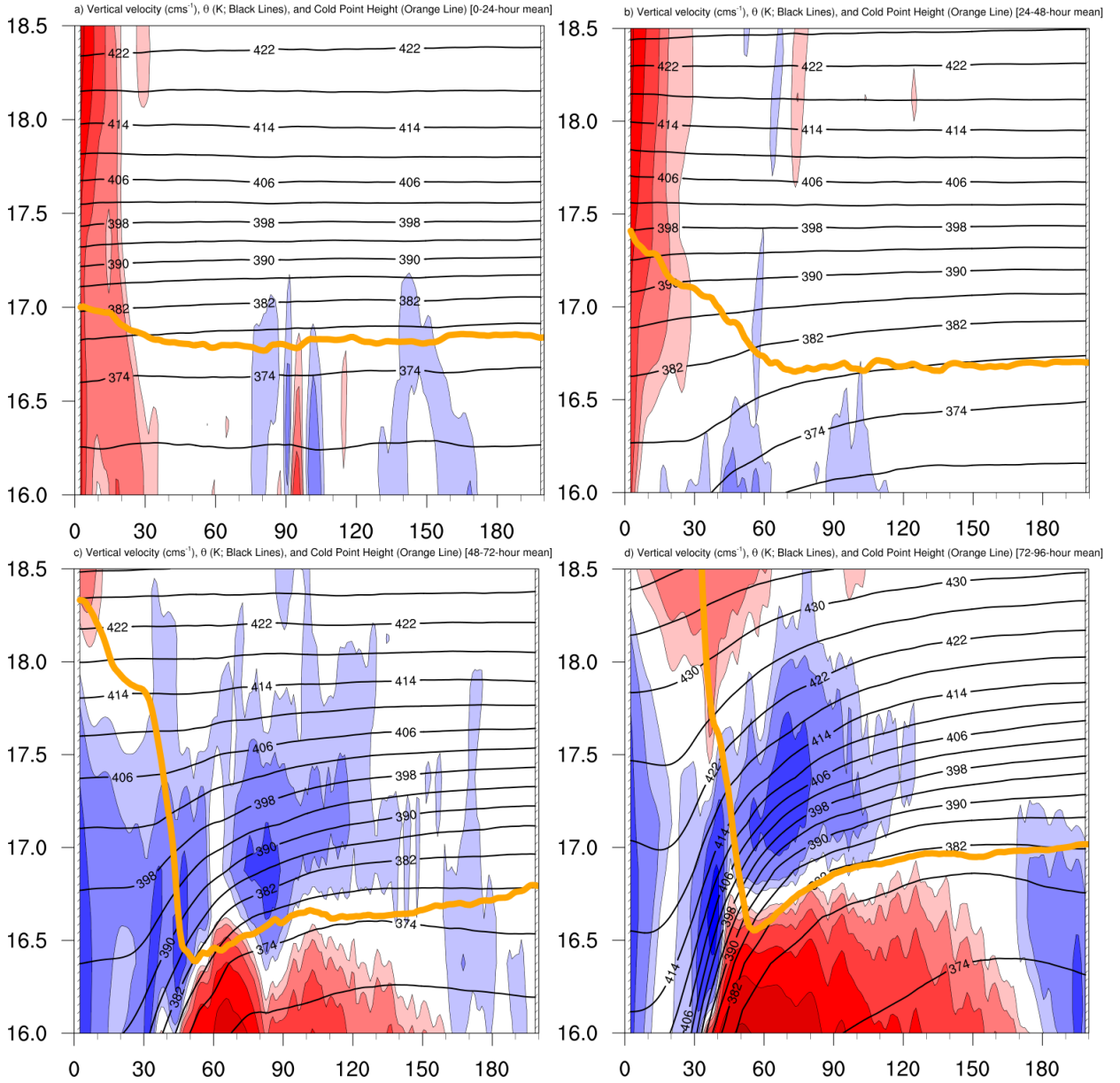
FIG. 10. Vertical velocity (cm s^{-1}; filled contours), potential temperature (K; thick black contours), and cold point tropopause height (orange line) averaged over (a) 0-24 hours, (b) 24-48 hours, (c) 48-72 hours, and (d) 72-96 hours.
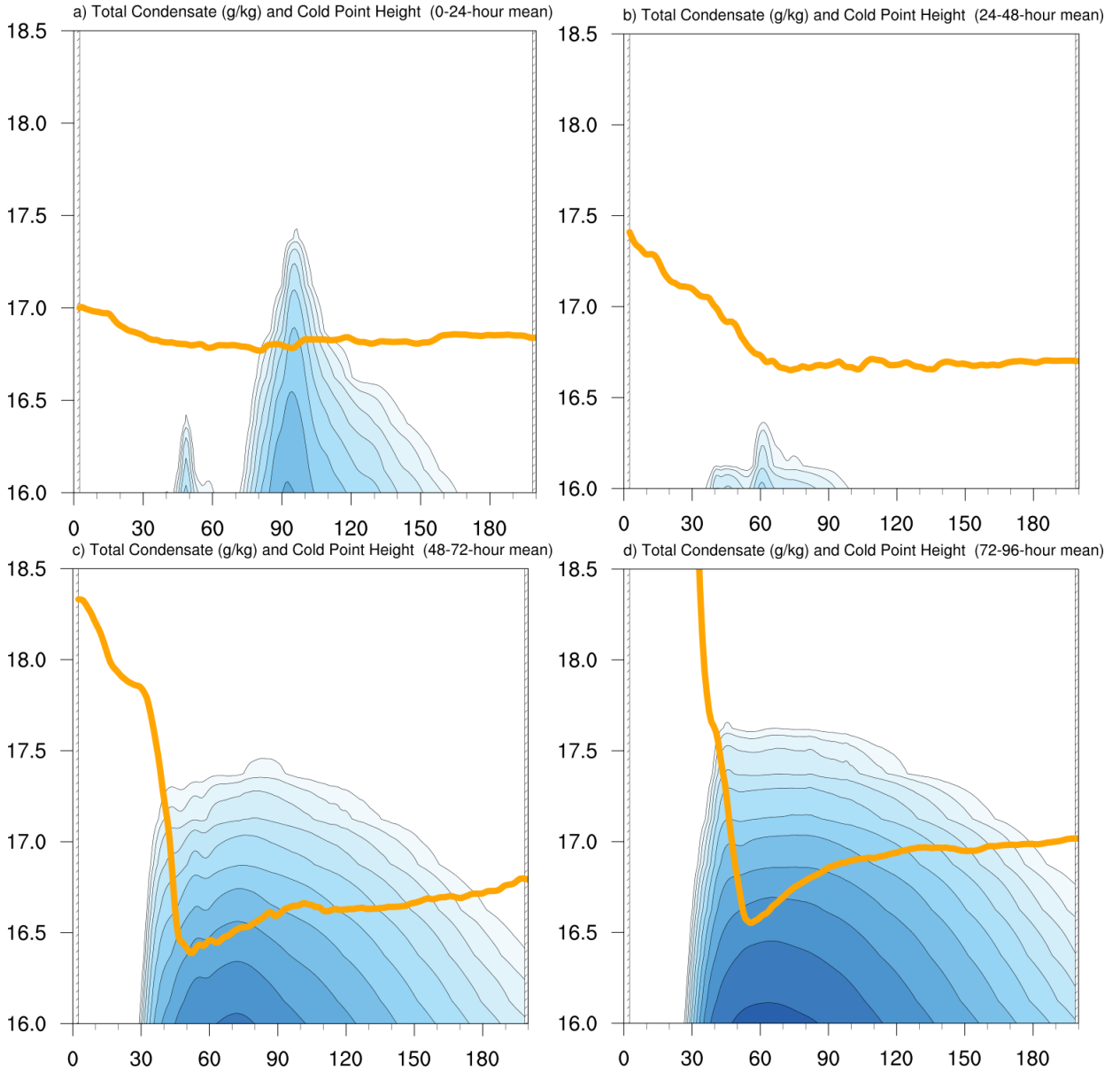
FIG. 11. Total condensate mixing ratio (g kg^{-1}) and cold point tropopause height (orange line) averaged over (a) 0-24 hours, (b) 24-48 hours, (c) 48-72 hours, and (d) 72-96 hours.